PHASE SEGMENTATION OPTIMIZATION OF MICRO X-RAY COMPUTED TOMOGRAPHY RESERVOIR ROCK IMAGES USING MACHINE LEARNING TECHNIQUES

HASAN ATRASH, FELICITASZ VELLEDITS

Institute of Mineralogy and Geology, University of Miskolc
hasan.alatrash87@gmail.com

Abstract: We studied the performance and accuracy of some basic segmentation techniques in the analysis of the pore space and matrix voxels obtained from a 3D volume of X-ray tomographic (XCT) grayscale rock images. The segmentation and classification accuracy of unsupervised (K-means, modified Fuzzy c-means, Minimum cross-entropy, and Type-2 fuzzy entropy) and supervised Naïve Bayes methods were tested using an XCT tomogram of a carbonate reservoir rock. K-fold- cross-validation techniques were applied in the evaluation of the accuracy of the unsupervised and supervised machine learning classifiers. The average porosity obtained was 31 ±6%, in good agreement with the ground truth image obtained by manual segmentation. In general, the accuracy of segmentation results can be strongly affected by the feature vector selection scheme, since it is difficult to isolate a particular machine learning algorithm for the complex phase segmentation problem. Therefore, our study provides a segmentation scheme that can help in selecting the appropriate machine learning techniques for phase segmentation.

Keywords: XCT imaging, porosity, image segmentation, machine learning

1. INTRODUCTION

Micro X-ray computed tomography (XCT) images of a reservoir rock sample can help in the characterization of pore space and assist in modeling pore-network geometries. A 3D pore-network representation can improve the understanding of the evolution of permeability and porosity of a rock sample [1]. X-ray computed tomography images, also known as tomograms, consist of a cubic array of reconstructed linear X-ray attenuation coefficient values (also known as pixel values). Accurate image segmentation is the first step toward pore-network modeling and analysis [2]. Image segmentation is the process of classifying similar values of image gray intensity into distinct groups or classes using machine learning (unsupervised or supervised) segmentation algorithm. Porous materials such as carbonates contain areas of void, called the pore space, as well as a number of distinct mineral components, each with a comparatively uniform density and consequently a similar gray value. There are some difficulties in acquiring a clear distribution separating the pore phase from the mineral phase. These difficulties arise from low density pore inclusions (e.g., microporosity, clays) below the image resolution, which make it difficult to distinguish between solid phase and the pore phase.

There have been intensive studies to improve segmentation methods for better quantitative characterization of pore space feature. Iassonov et al. [3] broadly classified segmentation algorithms into globally and locally adaptive segmentation. The fundamental concept behind the global thresholding scheme is that a single gray value is selected as a threshold value separating one phase from the other. There are many subcategories under the scheme, and the most commonly used is the histogram shape (triangulation) [4]. In locally adaptive segmentation the segmentation decision is made for each pixel taking into consideration the neighboring pixels. Utilization of local information helps in reducing the effects of some image artifact. One repeatedly used method is the probabilistic fuzzy c-means [5], which belongs to the unsupervised segmentation category but requires high computational power. In other works, such as Cortina-Januchs et al. [6], a combination of different algorithms is used where they applied clustering and artificial neural network (ANN) to segment binary soil images. whereas Khan et al. [7] used the supervised technique least-squares support vector machine (LS-SVM) for segmentation of XCT rock images.

Machine learning and neural networks were developed to mimic human sight and were initially used for speech and image recognition [8], [9]. They were soon used for the resolution enhancement of, for example, satellite images [10] and medical images [11] like magnetic resonance imaging [12] and computed tomography (XCT) [13].

Unsupervised learning is a machine learning technique where there is no need to supervise the model. Instead, the model is allowed to work on its own to discover information. It mainly deals with unlabeled data.

Supervised learning uses collected data or produces a data output from previous experience. It helps to optimize performance criteria using experience. A supervised learning model uses training data to learn a link between the input and the outputs. This link is used to sort out information, similarly to the training data from an unknown data set. Several algorithms can be used in the supervised approaches (e.g. support vector machine, neural network, linear and logistics regression, random forest, and classification trees). The classification and interpretation tasks determine which of the many available segmentation routines should be used [14].

In this paper, two unsupervised and two supervised methods were used to segment the pixels in the tomographic image. The unsupervised approaches were the K-means and the Fast and Robust Fuzzy c-Means (FRFCM) [15] clustering techniques. The supervised algorithms were two different entropy techniques: the Minimum Cross-Entropy (MINCE), and Type-2 Fuzzy Entropy (T2FE) algorithms. To compare the results and measure the accuracy of the segmentation, we applied two machine learning algorithms. They were the naïve Bayes classification and the 10 k-fold cross-validation algorithms.

The aims were to identify the classification scheme that (1) is best at segmenting the pore space and (2) is the most accurate for determining the porosity. A schematic illustration of the applied workflow is shown in *Figure 1*.
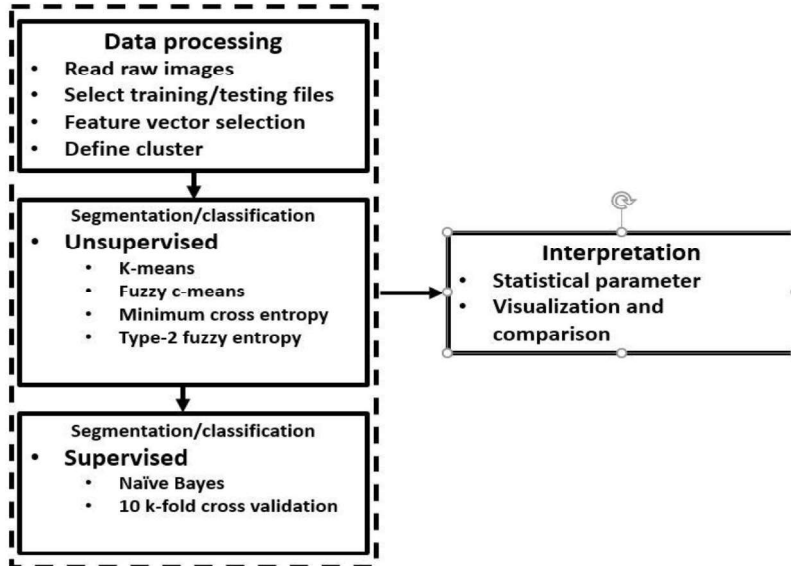
Figure 1
Flow chart describing the applied methodology

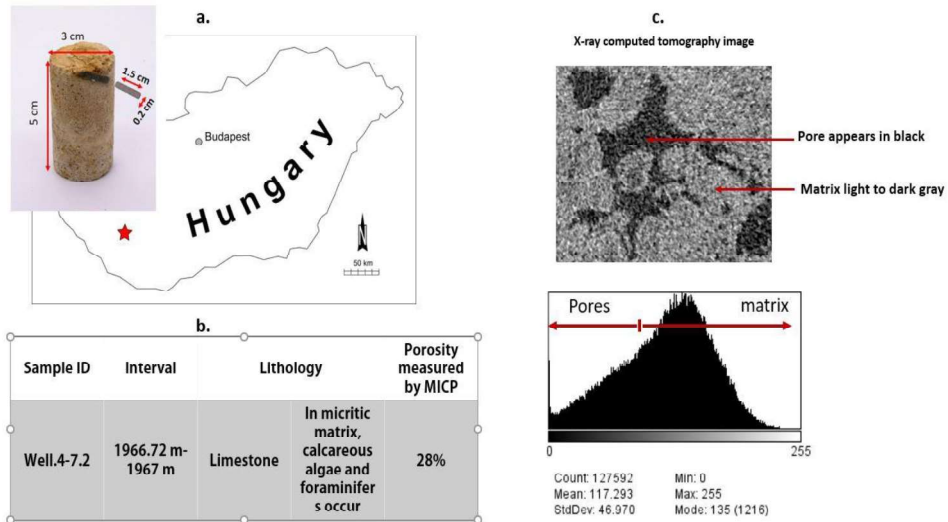## 2. MATERIALS AND METHODS

2.1. Rock sample

Figure 2
a. Are sample location and sample dimensions used for XCT scan,
b. sample depth lithology and measured porosity.
c. tomographic image used for this study and image histogram

For the analysis, a sample of shallow marine Sarmatian limestone [16] was used. The sample came from a cored section of a well drilled in the Mid-Hungarian Mega-Unit on the Northern part of the Somogy-Dráva basin, SW Hungary. The depth of the sample is 1967 m. The microscopic analysis showed a micritic matrix. Fossils such as foraminifers, algae, and other skeletal fragments were present in the sample [16]. The He porosity and Hg permeability were 28% and 55 mD, respectively. A cylindrical plug was taken from the main core with a diameter of 2 mm for μ-CT acquisition. The sample was scanned by micro CT. For the study, one tomogram was used. To avoid artifacts occurring on the edges of the scanned sample a subvolume was extracted for segmentation. The resolution of the extracted sub-volume lattice was 380 × 320 with a pixel size of 2 μm and pixel count of 127,592 *(Figure 2)*.

2.2. Thresholding by entropy

2.2.1. Thresholding using minimum cross entropy

Entropy is a thermodynamic quantity used in physics; it was introduced by German physicist Rudolf Clausius in the second half of the 18th century. It measures the disorder of a system and the spontaneous dispersal of energy as a function of temperature. In physics, the notion of entropy is typically regarded as a measure of the degree of randomness and the tendency of physical systems to become less and less organized. In 1870, Willard Gibbs gave a general entropy expression for a thermodynamic system as:

$$S = \sum_j P_j log P_j \qquad (1)$$

where Pj is the probability that the system is at state j. In 1877, Ludwig Boltzmann quantified entropy of an equilibrium thermodynamic system as:

$$S = K \cdot log W, \qquad (2)$$

where S is entropy, K is the Boltzmann constant, and W is the number of states in the system.

In 1949, Claude Shannon redefined the entropy concept of Boltzmann/Gibbs as a measure of uncertainty regarding the information content of a system [17]. In information theory, entropy measures the amount of uncertainty of an unknown or random quantity [18].

Many entropy-based thresholding methods exist in the literature. These methods can be categorized into three groups: entropic thresholding, cross-entropic thresholding, and fuzzy entropic thresholding [18]. Cross-entropic thresholding formulates the thresholding as the minimization of an information-theoretic distance [19]. Entropy could be used also as "a measure of separation that separates the information into two regions, above and below an intensity threshold" [20]. Entropic thresholding considers "the image foreground and background as two different signal sources so that when the sum of the two-class entropies reaches its maximum, the image is said to be optimally thresholded" [19]. When the minimum cross-

entropy criterion is applied to threshold segmentation, it refers to searching for the threshold that can minimize the information content before and after segmentation.

The simplest and most direct scheme for threshold selection would be to iterate through all possible threshold values and to select th threshold that corresponds to the minimum of the cross-entropy.

2.2.2. Type-2 fuzzy entropy thresholding:

A classical set *A* can be defined as a collection of elements that can either belong to or not belong to set *A*. In contrast, a fuzzy set is a collection of objects without clear boundaries or well-defined characteristics. There are two types of fuzzy sets. A Type-I fuzzy set *A*, in a finite set, $X = \{x_1, x_2, \ldots, x_n\}$ may be represented as in *Equation (3)*:

$$A = \{x, \mu_A(x) \mid x \in X, 0 \le \mu_A(x) \le 1\}, \tag{3}$$

where $0 \le \mu_A(x) \le 1$ and $\mu_A(x)$ is called the membership function, which measures the closeness of x to A and which can only take a single value. In a Type-2 fuzzy set, a range of membership values is used instead of a single value. If *A* is a Type-2 fuzzy set, then:

$$A = \{x, \mu_A^{High}(x), \mu_A^{Low}(x) \mid x \in X, 0 \le \mu_A^{High}(x), \mu_A^{Low}(x) \le 1\}, \tag{4}$$

In the above definition, μ_A^{High}, and μ_A^{Low} are the upper and lower membership functions, respectively.

A digital image, I_{Gr}, contains $M \times N$ pixels, where each pixel has a position defined by (m; n). The image has L intensity values that are stored in the pixels. In this context, the distribution of the intensity levels on the image can be represented by a histogram that can also be normalized as $H = \{h_0, h_1, \ldots, h_{L-1}\}$. Each value, h_i, is computed using *Equation (5)*:

$$h_i = \frac{np_i}{(NP)}, \ \sum_{i=1}^{NP} h_i = 1, \tag{5}$$

where i is a level of intensity $(0 \le i \le L - 1)$ and $NP = M \cdot N$ is the total number of pixels contained in the image. The term ultra-fuzziness can be used as a metric associated with a fuzzy set. It gives a 0 value when the membership values can be represented without any uncertainty. However, the value rises to 1 when membership values can be specified within an interval. For a digital image, the ultra-fuzziness for the ith level of intensity is defined as

$$P_k = \sum_{i=0}^{L-1} (h_i * (\mu_k^{high}(i) - \mu_k^{low}(i))), \ K = \{1, 2, \ldots, nl\} \tag{6}$$

Fuzzy entropy measure is a concept used to assess the amount of vagueness within a fuzzy set. The type II fuzzy entropy for a kth −threshold is therefore given as:

$$Fe_k = -\sum_{i=1}^{L-1} \left(\frac{(h_i * (\mu_k^{high}(i) - \mu_k^{low}(i)))}{P_k} \right) * in \left(\frac{(h_i * (\mu_k^{high}(i) - \mu_k^{low}(i)))}{P_k} \right), K = \{1, 2, \ldots, nl\}, \tag{7}$$

The sum of all the entropies for the $(nl + 1)$ levels is the total entropy defined as:

$$T_{Fe}(a_1, c_1, \ldots, a_n, c_n) = \sum_{k=1}^{nt+1} Fe_i, \qquad (8)$$

2.3. Image thresholding by clustering

2.3.1. K-means thresholding

Cluster analysis is a concept used to organize observed data into a meaningful structure by discovering the natural grouping(s) of a set of patterns, points, or objects, to gain further insight from them. In such a structure, the similarities between objects in the same group are high while the similarities between objects in different groups are low.

Hierarchical clustering is a method of cluster analysis where the algorithm builds a hierarchy of clusters either in agglomerative or divisive mode. In the cases of partitional clustering algorithms, the algorithms find all the clusters simultaneously, as a partition of the data, and do not impose a hierarchical structure. The most popular and simplest partitional algorithm is K-means clustering [21]. It is a simple unsupervised learning procedure. The calculation consists of two separate phases. The first phase is for the initializing K centroids. In the second phase, each data point is assigned to its closest centroid. The initial centroids are iteratively updated to the mean of the constituent data points. The algorithm finally converges when no further change occurs in the assignment of data points to the centroids. In this state, the points in any cluster have a minimum distance to the corresponding centroid. Several methods can be used to define the distance of the nearest centroid. Among them, Euclidean distance is one of the most frequently used approaches.

2.3.2. Fuzzy c-means clustering (FCM)

FCM is superior to hard clustering as it has more tolerance to ambiguity and retains more original image information [15]. The concept of characterizing an individual point's similarity to all the clusters was introduced by Zadeh (1965) [22]. The key to Zadeh's idea is to depict the similarity a point shares with each cluster by a membership function. Additionally, the sum of the memberships for each sample point must be unity. Each sample will have a membership in every cluster. Memberships close to unity signify a high degree of similarity between the sample and a cluster, while memberships close to zero imply little similarity between the sample and that cluster. The net effect of such a function for clustering is to produce fuzzy c-partitions of a given data set [22]. FCM value uses an iterative optimization of an objective function based on a membership function [23]. A local extremum of this objective function indicates an optimal clustering of the input data [24].

FCM has been used in image segmentation [25] [15], and it proved effective for images with simple texture and background [15]. Nonetheless, it fails to segment images with complex textures and background or images corrupted by noise because it only considers gray-level information without considering the spatial information

[15]. To resolve the problem, one popular idea is to incorporate the local spatial information in an objective function to improve the segmentation effect [15]. Lei et al. [15] proposed an improved FCM algorithm based on morphological reconstruction, and membership filtering (FRFCM). By introducing a morphological reconstruction operation, the algorithm manifests tolerance to the noise presented in the image. Consequently, image details are preserved. In the next step, the membership partition is replaced by membership filtering that depends only on the spatial neighbors of the membership partition [15].

The FRFCM algorithm can be summarized as follows:

Step 1: Set the cluster prototype value, fuzzification parameter, the size of the filtering window, and the minimal error threshold.

Step 2: Compute the new image and then compute the histogram of that image.

Step 3: Initialize randomly the membership partition matrix.

Step 4: Update the clustering centers.

Step 5: Update the membership partition matrix.

2.4. Supervised learning classifier

In supervised learning classifiers only labeled data (training patterns with known category labels) are involved. A supervised classifier is trained using a set of pre-defined features or classes (known as training data), where similar pixel values are sorted out from unknown data set (testing data) using supervised learning techniques. The performance of this classifier on the testing subset(s) indicates the stability of the clustering algorithm.

2.4.1. Naïve Bayes classifier

Treating image properties as random variables, and deriving a probabilistic model based on Bayesian decision theory [26] provides the foundation for Bayesian image segmentation. The motivation for the application of a stochastic framework is based on the assumption that the variation and interactions between image attributes can be described by probability distributions [27]. The naïve Bayes classifier is based on Bayes' theorem [28].

Bayes' theorem says that the probability that an event x belongs to a class k can be calculated by using the following equation:

$$P(c_k|\text{x}) = \frac{P(\text{x}|c_k)P(c_k)}{P(\text{x})}, \tag{9}$$

In *Equation (9)*, $P(c_k|\text{x})$ is a posterior probability, $P(\text{x}|c_k)$ is the probability of x occurring given evidence c_k has already occurred, $P(c_k)$ is the Probability of c_k occurring, $P(\text{x})$ is the probability of x occurring. Based on the Bayesian decision we can decide the optimum class k for the event x by choosing the class with the highest probability among all possible classes. This choice can minimize the classification error [27]. For doing so, we need to estimate $P(\text{x}|c_k)$ providing that any particular value of vector x conditional on c_k is statistically independent of each dimension [27]:

$$P(x|c_k) = \prod_{i=0}^{n} P(x_i|c_k), \qquad (10)$$

where x is a n-dimensional vector.

The naïve Bayes classifier can then be calculated as:

$$K = \text{argmax}_k \, p(c_k) \prod_{i=0}^{n} P(x_i|c_k), \qquad (11)$$

2.5. Model evaluation metrics and accuracy assessment

In classification problems there are several evaluation metrics to assist the classification accuracy. These metrics can be described as follows:

K-fold cross validation: The idea for cross-validation was first proposed by Larson (1931) [29]. Cross-validation is a statistical method of evaluating and comparing learning algorithms. It divides the data set into two subsets: one is used to learn or train a model and the other is used to validate the model. The problem with such a model is that it may demonstrate adequate prediction capability on the training data, but it might fail to predict future unseen data [1]. There are several approaches to estimate the accuracy of classifiers using different combinations of k-fold cross-validation techniques. Kohavi (1995) [30] and Dietterich (1998) [31] recommended 10-fold cross-validations as one of the best cross-validation techniques, as it mitigates biases despite variances in the size of training and testing datasets. At the onset of 10 k-fold cross-validations, the dataset is initially stratified and partitioned into 10 equal (or nearly equal) subsets or folds. Subsequently, 10 iterations of training and validation are performed such that, within each iteration, a different fold of the data is held out for validation, while the rest of the folds are used for learning. A schematic illustration of the workflow of 10 k-fold cross-validations in conjunction with naïve Bayes is shown in *Figure 3*.
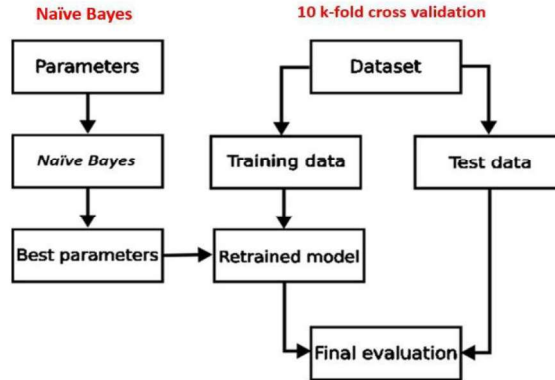

Figure 3

Schematic illustration of supervised machine learning algorithm using naïve Bayes and 10 k-fold cross validation. On the left side are the parameters resulting from the naïve Bayes classifier, and on the right side the data trained and tested, and the final evaluation is done using 10 k-fold cross validation

Precision is the proportion of positive cases that were correctly identified. The precision is the ratio tp / tp + tf, where tp is the number of true positives (positive cases that were correctly identified) and fp is the number of false positives (negative cases identified as positive). Recall is the proportion of actual positive cases which are correctly identified. F1 is the harmonic mean of precision and recall values for a classification problem. Area under ROC curve: the ROC (Receiver operating characteristic) curve is the plot between sensitivity and (1-specificity). (1-specificity) is also known as false positive rate and sensitivity is also known as the true positive rate. To bring this curve down to a single number, we find the area under this curve (AUC). Classification accuracy (CA) measures the number of correct predictions made divided by the total number of predictions made.

3. RESULTS

3.1. Image segmentation and segmentation accuracy

The classification process intends to categorize every pixel in a digital image. Each class of pixels is based on a specific feature. The categorized data could then be used to retrieve useful information. In this study, these classes were applied to compute porosity and assist in the calculation of pore size distribution.

One of the main challenges for the comparison of segmentation algorithms for X-ray CT images of porous materials is the lack of ground truth, i.e. the lack of knowledge of the optimal binarization result. Generally, two basic methods are applied to the objective evaluation of image segmentation: an analytical technique or an experimental technique [32].

The analytical technique evaluates an image segmentation algorithm by analyzing the principle of the algorithm. The experimental technique, which is widely used, interprets and compares experimental results of image segmentation algorithms to make an evaluation, and it can be subdivided into two distinct methods: superiority evaluation method and deviation evaluation method [33].

The superiority evaluation method evaluates an image segmentation algorithm by utilizing human visual traits [34]. In the deviation evaluation method, firstly a standard segmentation image is provided for comparison criteria. Then the disparity between actual segmentation and ideal one can be calculated to evaluate the image segmentation algorithm [35].

In the experimental technique, the different image segmentation algorithm is tested and compared in terms of four criteria: visual comparison, calculated pore size, pore volume, and pore count. Finally, the results are compared to a ground truth segmented image, where the latter is obtained by manual labeling of the pixels of the tested image based on the visual evaluation. It is worth mentioning that a ground truth image is not necessarily an optimal segmentation since the evaluation of the ground truth image is done visually. An additional datum assists in making the final decision.

For segmentation one XCT tomogram with the dimension of 320 × 380 was used. This tomogram was the best representation of the pore phase. The segmented images

were created by using k-means, fast and robust fuzzy c-means, minimum cross-entropy, type-2 fuzzy entropy, and the naïve Bayes classifier. In the letter case, all the available features were grouped into two groups. Each group had homogeneous features (in our case pores and matrix) and formed a feature vector. The whole dataset was used in the training the classifier. To test the classifier and to avoid data overfitting, a 10 k-fold cross-validation was implemented. In that process, the data was stratified and divided into 10 folds. One fold was held out for testing and validation, and the other nine were for the training. This process was repeated for each fold iteratively.

The naïve Bayes method classified the rock image into the pore phase and solid phase. This result was tested using each of the segmentation algorithms mentioned above. The classification accuracy resulting from each training was relatively high. This was reasonable since the unidentified threshold value was confined within a limited gray intensity range which was mainly represented by the transition zone lying in between the two phases.

Nevertheless, the set of misclassified pixels detected by the supervised machine learning algorithm for each training set varied. In fuzzy c-Means and type 2 fuzzy entropy, the number of the misclassified pixels was the highest. The reason for that could be attributed to the fact that in fuzzy classification, a single gray value could be a member of more than one group at the same time. In contrast, the naïve Bayes algorithm does not consider special location. Classification accuracy in the naïve Bayes classifier is listed in *Table 1*. The resulting binarized images for each segmentation method are shown in *Figure 4*.

Table 1

Comparison of classification accuracy on naïve Bayes classifier with different feature vectors

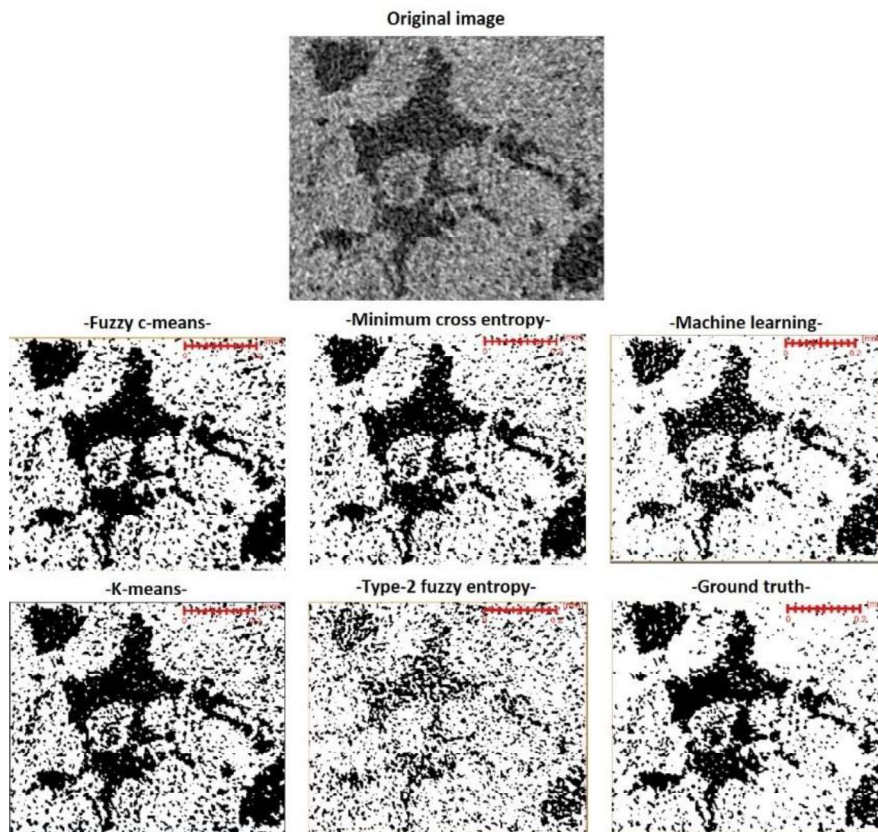| Classifier	AUC	CA	F1	Precession	Recall	Misclassified	Misclassified pixels gray range	Naïve Bayes Predicted Threshold value
K-means	0.965	0.877	0.871	0.897	0.877	15600	85-107	85
Fuzzy c-means	0.967	0.888	0.882	0.904	0.888	40310	85-104	85
Minimum cross entropy	0.974	0.946	0.944	0.95	0.946	6941	85-91	85
Fuzzy entropy	0.984	0.965	0.965	0.967	0.965	18064	85-112	103

Figure 4
2-D segmented images and binarized using unsupervised and supervised
segmentation where pores appear in black and matrix in white

3.2. Evaluation and comparison

The performances of the unsupervised and supervised classification methods are evaluated in terms of how well they classified the pore phase pixels in the XCT images. The volume fraction and pore counts are shown in *Figure 5*. The K-means and FRFCM clustering tend to over-segment the pore volume by 7% to 12% compared to other segmentation algorithms, where pore volume varies between 25% and 30%.

This variability in pore volume can be attributed to the presence of microcrystalline cement formed during diagenetic processes at the microstructural scale and deposited within the void space and on the pore edges, which cannot be resolved by the XCT. This situation leads to images having variable pixel intensities including the pore edges. These pixels of varying intensities would not have been segmented into the same classes by different machine learning algorithms. The aforementioned microcrystalline cement has been observed by microscopic examination of the thin sections taken from the same samples *(Figure 6)*. In *Figure 6*, we also compare

tomograms to thin sections and depicted similar attributes in both images in terms of complex pore shapes and pore distribution.

We used the calculated entropy to determine what fraction of the image needs to be carefully segmented. Image entropy is shown in *Figure 7*. The threshold window was determined by Gaussian curve fitting over the range between 82 and 138 *(Figure 7)*.
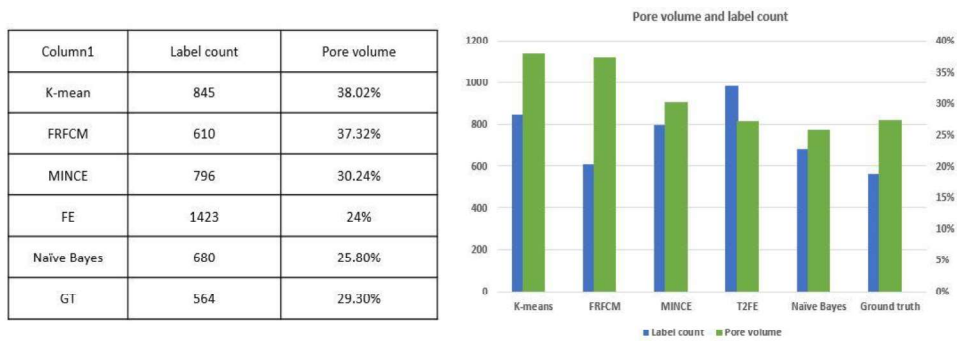
Column1	Label count	Pore volume
K-mean	845	38.02%
FRFCM	610	37.32%
MINCE	796	30.24%
FE	1423	24%
Naïve Bayes	680	25.80%
GT	564	29.30%

Figure 5
*Porosity values and pore count obtained by using unsupervised
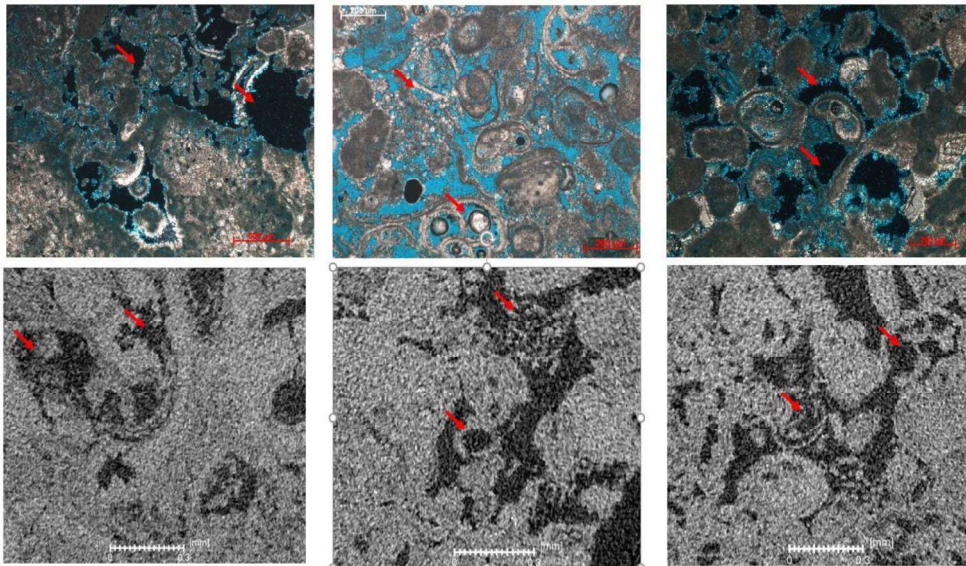and supervised classifiers*

Figure 6
*Visual inspection between thin sections (upper raw) and tomograms (lower raw).
In the upper raw are microscopic images of thin sections taken from the sample.
Grains appear in light whitish are microcrystalline cement, which also darkened
in other places based on crystal orientations. The lower raw are XCT tomograms
for the same sample. The arrows indicates to pore constituent in both images.*
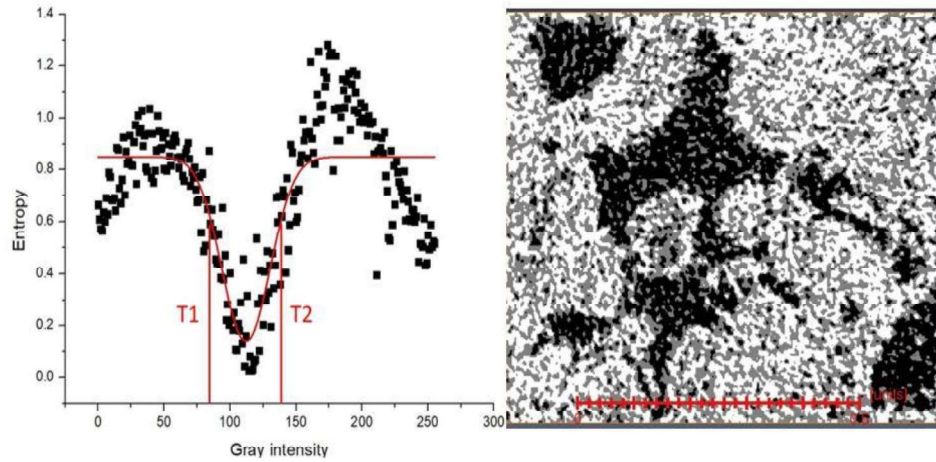
Figure 7

*Studied image entropy measure where entropy appears in black and the red curve
is Gaussian fit, T1 and T2 are the boundaries of the fuzzy interval determined
by Gaussian at 82 and 138, respectively. The image to the right is an illustration
for the fuzzy interval where the original image labeled where the pixels within 82
and 132 range appear in light gray, pores are in black and matrix in white.*

The porosities were calculated using different segmentation algorithms *(Figure 5)*.
In our case, the porosity was defined as the ratio between the pore phase voxels and
the entire sample volume and expressed in percentage. The measured pore volume
using unsupervised clustering techniques K-means and fuzzy c-means agree with
each other, yet the pore counts were different. In type 2 fuzzy entropy small pores
are more frequent compared to big pores, resulting in higher pore counts and lower
pore volume compared to clustering and minimum cross entropy. In ground truth
and the naïve Bayes classifier the measured pore volume and pore counts show
approximately similar values.

The geometrical pore size distribution was calculated from the 8-bit segmented
images using Avizo software. The pore sizes were determined by the morphological
approach. This method fits spheres into the pores. The resulting pore size
distributions coming from the different segmentation methods are shown in *Figure
8*. The calculations of P10, P50, and P90 values percentiles allowed the interpretation
of geometrical pore size distribution in the terms of the micro- and macro-pore
contributions to the total pore volume *(Table 2)*. *Figure 8* and *Table 2* show that
segmentation by K-means clustering and MINCE the detected pores counts of the
K-means clustering the MINCE methods are higher than those of the other methods.
In the case of the T2FE, the small pores are more frequent than the big ones.
However, in the case of FRFCM algorithm, the big pores are more dominant. The
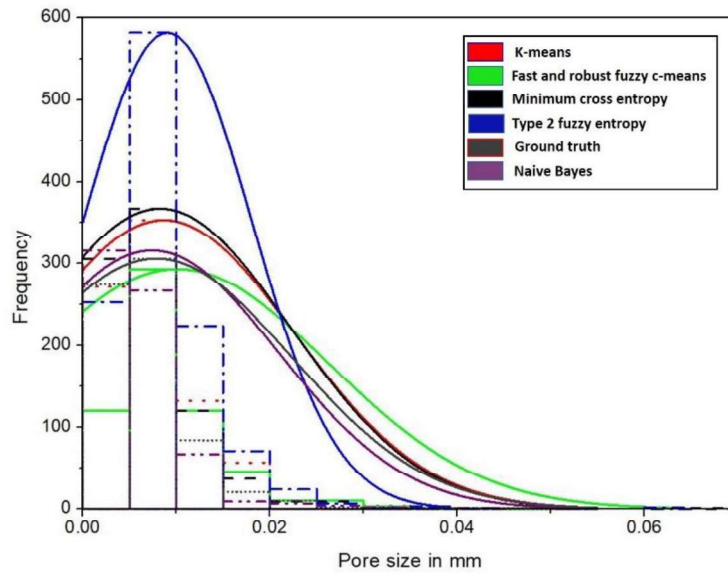Ground truth and Naïve Bayes show similar pore size distribution.

Figure 8
Histogram and normal curve for pore size distribution
for each segmentation method

Table 2
Pore size diameter obtained for six segmentation algorithms

Classifier algorithm	D10 mm	D50 mm	D90 mm
K-means	0.00226	0.00638	0.01514
FRFCM	0.00391	0.00748	0.01596
MINCE	0.00226	0.00597	0.01373
T2FE	0.003909	0.007137	0.01497
Naïve Bayes	0.00226	0.00505	0.01131
Ground truth	0.00391	0.00677	0.01329

4. CONCLUSION

We have discussed some of the basic image segmentation algorithms. Also, we evaluated the quality of the image segmentation and the accuracy of the classifications. Our analyses showed that the K-means and MINCE algorithms performed well and gave good accuracy scores. The FRFCM and T2FE tended to over-segment the pore space. In the supervised machine learning method, the results were more realistic in comparison to other segmentation results and to the original image and ground truth image.

REFERENCES

[1]   Chauhan, S., Rühaak, W., Anbergen, H., Kabdenov, A., Freise, M., Wille, T., Sass, I. (2016). Phase segmentation of X-ray computer tomography rock images using machine learning techniques: An accuracy and performance study. *Solid Earth*, 7 (4), pp. 1125–1139. https://doi.org/10.5194/se-7-1125-2016

[2]   Gonzalez, R. C., Woods, R. E. (2008). *Digital Image Processing.* 3rd Edition. Upper Saddle River, NJ: Pearson, Prentice-Hall.

[3]   Iassonov, P., Gebrenegus, T., Tuller, M. (2009). Segmentation of X-ray computed tomography images of porous materials: A crucial step for characterization and quantitative analysis of pore structures. *Water Resources*, Volume 45, pp. 1–12, https://doi.org/10.1029/2009WR008087.

[4]   Zack, G.W., Rogers., W., Latt, S. (1977). Automatic measurement of sister chromatid exchange frequency. *J. Histochem. Cytochem*, 25, pp. 741–753. https://doi.org/10.1177/25.7.70454

[5]   Pham, T. (2001). Image segmentation using probabilistic fuzzy c- means clustering. *Proc., 2001 IEEE International Conference on Image Processing*, Vol. 1, pp. 722–725, https://doi.org/10.1109/ICIP.2001.959147.

[6]   Cortina-Januchs, M., Quintanilla-Dominguez, J., Vega-Corona, A., Tarquis, M., Andina, D. (2011). Detection of pore space in CT soil images using artificial neural networks. *Biogeosciences*, 8, pp. 279–288. https://doi.org/10.5194/bg-8-279-2011.

[7]   Khan, F., Enzmann, F., Kersten, M. (2016). Multi-phase classification by a least-squares support vector machine approach in tomography images of geological samples. *Solid Earth*, 7, pp. 481–492. https://doi.org/10.5194/se-7-481-2016

[8]   Fukushima, K. (1980). A self-organizing neural network model for a mechanism of pattern recognition unaffected by shift in position. *Biol. Cybermetics*, 36, pp. 193–202, https://doi.org/10.1007/BF00344251.

[9]   [9] Lecun, Y., Bengio, Y., Hinton., G. (2015). Deep learning. *Nature*, 521, pp. 436–444, https://doi.org/10.1038/nature14539.

[10]   Chang, Y., Luo, B. (2019). Bidirectional convolutional LSTM neural network for remote sensing image super-resolution. *Remote Sensing*, 11, pp. 1–18. https://doi.org/10.3390/rs11202333

[11]   Kaji, S., Kida, S. (2019). Overview of image-to-image translation by use of deep neural networks: Denoising, super-resolution, modality conversion, and reconstruction in medical imaging. *Radiological Physics and Technology*, 12, pp. 235–248, https://doi.org/10.1007/s12194-019-00520-y.

[12] Pham, C., Tor-Díez, C., Meunier, H., Bednarek, N., Fablet, R., Passat, N., Rousseau, F. (2019). Multiscale brain MRI super-resolution using deep 3D convolutional networks. *Computerized Medical Imaging and Graphics*, 77, pp. 1–15, https://doi.org/10.1016/j.compmedimag.2019.101647.

[13] You, C., Li, G., Zhang, Y., Zhang, X., Shan, H., Li, M., Ju, S., Zhao, Z., Zhang, Z., Cong, W., et al. (2019). CT Super-resolution GAN Constrained by the Identical, Residual, and Cycle Learning Ensemble. *(GAN-CIRCLE). IEEE Trans. medical imaging*, 39, pp. 188–203.
https://doi.org/10.1109/TMI.2019.2922960

[14] Chauhan, S., Rühaak, W., Khan, F., Enzmann, F., Mielke, P., Kersten, M., Sass, I. (2016). Processing of rock core microtomography images: Using seven different machine learning algorithms. *Computers and Geosciences*, 86, pp. 120–128, https://doi.org/10.1016/j.cageo.2015.10.013.

[15] Lei, T., Jia, X., Zhang, Y., He, L., Meng, H., Nandi, K. (2018). Significantly Fast and Robust Fuzzy C-Means Clustering Algorithm Based on Morphological Reconstruction and Membership Filtering. *IEEE Transactions on Fuzzy Systems*, 26 (5), pp. 3027–3041.
https://doi.org/10.1109/TFUZZ.2018.2796074

[16] Mukhtar, T. (2020)*. Sedimentological Control on the Productive and Dry Intervals in Four Investigated Wells.* Master Thesis, University of Miskolc.

[17] Sengur, A., Turkoglu, I., Ince, M. (2006). A Comparative Study On Entropic Thresholding Methods. *Journal of Electrical & Electronics Engineering*, 6 (2), pp. 183–188.

[18] Mahmoudi, L., El Zaart, A. (2012). A survey of entropy image thresholding techniques. *Proc., 2012 2nd International Conference on Advances in Computational Tools for Engineering Applications, ACTEA*, pp. 204–209.
https://doi.org/10.1109/ICTEA.2012.6462867

[19] Sezgin, M., Sankur, B. (2004). Survey Over Image Thresholding Techniques And Quantitative Performance Evaluation. *Journal of Electronic Imaging*, 13 (1), pp. 146–165.

[20] Al-Attas, R., El-Zaart, A. (2006). Thresholding of Medical Images Using Minimum Cross Entropy, *Proc., Kuala Lumpur International Conference on Biomedical Engineering*, Kuala Lumpur, Malaysia, pp. 312–315.

[21] Jain A. (2010). Data clustering: 50 years beyond K-means. *Pattern Recognition Letters,* 31 (8), pp. 651–666.

[22] Zadeh, A. (1965). Fuzzy sets. *Information and Control*, 8 (3), pp. 338–353.

[23] Toz, G., Yücedağ, İ., Erdoğmuş, P. (2019). A fuzzy image clustering method based on an improved backtracking search optimization algorithm with an

inertia weight parameter *Journal of King Saud University - Computer and Information Sciences*, Vol. 31 (3), pp. 295–303.

[24] Nikhil, R., Sankar, K. (1993). A review on image segmentation techniques. *Pattern Recognition*, Vol. 26, pp. 1277–1294.

[25] Choudhry, M., Kapoor, R. (2016). Performance analysis of fuzzy c-means clustering methods for MRI image segmentation. *Procedia Computer Science*, Vol. 89, pp. 749–758

[26] Duda, R., Hart, P. (1973). *Pattern Recognition and Scene Analysis*. New York, Wiley-Interscience.

[27] Dong-Chul, P. (2016). Image Classification Using Naive Bayes Classfier. *International Journal of Computer Science and Electronics Engineering*, 4 (3), pp. 2320–4028.

[28] Jang, M., Park, D. (2016). Stochastic Classifier Integration Model. *International Journal of Applied Engineering Research*, 11 (2), pp. 809–814.

[29] Larson, C. (1931). The shrinkage of the coefficient of multiple correlation. *J. Educ. Psychol.*, Vol. 22, pp. 45–55, https://doi.org/10.1037/h0072400.

[30] Ron, K. (1995). A study of cross-validation and bootstrap for accuracy estimation and model selection. *Proc., The International Joint Conference on Artificial Intelligence (IJCAI)*, pp. 1137–1145.

[31] Dietterich, T. (1998). Approximate statistical tests for comparing supervised classification learning algorithms, *Neural Computation*, 10 (7), pp. 1895–1923.

[32] Sharon, E., Brandt, A., Basri, R. (2000). Fast multiscale image segmentation. *Proc., IEEE Conference on Computer Vision*, Vol. 1, pp. 70–77.

[33] Brink, D. (1992). Thresholding of digital images using of two-dimensional entropies. *Pattern Recognition*, 25 (8), pp. 803–808.

[34] Zhou, L., Gao, X. (2004). Image segmentation via fast fuzzy c- means clustering. *Computer Engineering and Application*, 40 (8), pp. 68–70.

[35] Wang, Q. (1998). One image segmentation technique based on wavelet analysis in the context of texture. *Data Collection and Processing*, 13 (1), pp. 12–16.